Computational Particle Mechanics
https://doi.org/10.1007/s40571-025-01061-5

Modelling the breakage of coated particles using discrete element and bonded particle method

Wasif Safdar[1] · **Sonja Rotter**[1] · **Maike Orth**[2] · **Stefan Heinrich**[2] · **Alexander Düster**[1]

Received: 29 April 2025 / Revised: 7 August 2025 / Accepted: 11 August 2025

Abstract
In recent years, particles have gained popularity as crash absorbers. To improve their mechanical properties, a coating layer can be applied. To predict the effect of this coating, a numerical model must be developed. For this purpose, the present study employs the discrete element method, extended by the bonded particle method, using both high- and low-fidelity approaches. In this framework, a single physical particle is modelled as a cluster or agglomerate of smaller particles bonded together. To identify the parameters involved, a sensitivity analysis is performed, followed by optimisation using the particle swarm algorithm, with calibration based on uniaxial single particle compression tests. Once an optimised parameter set is obtained, the models are validated against multi particle compression test results. The outcomes of this study demonstrate the potential of the proposed methodology for simulating large-scale compression tests of coated granular materials.

Keywords Discrete element method · Bonded particle method · Breakage · Fidelity · Cost

1 Introduction

The use of granular media has gained significant interest in recent years as a medium for energy absorption and damping [10, 20]. This is particularly beneficial in the field of ship design, as illustrated in [23, 24], where a ship's double hull was filled with particles. These particles dissipate energy through crushing. Furthermore, the entire structure behaves like a sandwich beam, which facilitates the transfer of load from the outer to the inner hull. As a result, the ship's crashworthiness is improved. This is important for several reasons, including enhanced safety for crew and passengers, protection of the environment, such as preventing catastrophic oil spillages, and the economic implications associated with repair costs.

Previous studies have shown that lightweight expanded glass granules, such as Poraver®, made from recycled glass, are particularly suitable due to their properties, including being lightweight, non-flammable, hydrophobic and non-toxic [29]. However, a key challenge remains: under cyclic loading, the granules are crushed into fine dust. Consequently, their mechanical performance is reduced due to abrasion and variability in breakage behaviour. One approach to overcome this is to apply a coating layer around the particles [14]. This additional layer improves the mechanical strength, energy absorption capacity and resistance to abrasion. Additionally, the formation of dust was significantly reduced from 14.6% to less than 0.5% when coated particles were used in a cyclic loading test. Moreover, multi particle compression tests showed, as mentioned above, higher energy absorption and strength compared to uncoated particles. Importantly, these advantages were achieved while maintaining a low overall density, preserving the lightweight nature of the material. These findings confirmed that coated particles are promising when used as crash absorbers in a ship's double hull.

In order to predict the crushing behaviour of coated particles on large-scale experiments, a numerical model needs to be developed. Although physical experiments provide an accurate picture, they are costly, time consuming and difficult to realise due to need for specialised equipment, complex test setups, and large material quantities. Moreover, they offer limited flexibility for studying the influence of individual parameters, such as the effect of coating on particle breakage

---

✉ Wasif Safdar
wasif.safdar@tuhh.de

[1] Numerical Structural Analysis with Application in Ship Technology (M-10), Hamburg University of Technology, 21073 Hamburg, Germany

[2] Institute of Solids Process Engineering and Particle Technology (SPE), Hamburg University of Technology, 21073 Hamburg, Germany

in a double hull experiment. Therefore, a reliable numerical model is needed to generalise and explore larger parameters space. For this purpose, the discrete element method (DEM) is a natural choice since it simulates particle motion using Newton's laws. However, these particles are treated as quasi-rigid bodies. To be able to simulate the breakage of particles, DEM can be extended using the bonded particle method (BPM), wherein each physical particle is represented by a cluster of smaller particles bonded together [18]. When a failure criterion is reached, the bonds break, which simulates the physical particle's crushing behaviour. This DEM-BPM approach has been applied successfully to simulation showing crack initiation and propagation [2–4].

In this work, we develop a DEM-BPM model to simulate the breakage of coated particles using the open-source code MUSEN [6]. The model is calibrated using experiments of single and multi particle tests using sensitivity analysis and particle swarm algorithm (PSO) to determine an optimised set of parameters. Since a high-fidelity approach is computationally expensive, we propose a low-fidelity approach that exhibits a similar mechanical response for a lower computational cost with the aim of performing large-scale simulations, for example double hull simulation, in the future.

2 Coated particles

The particles considered in this study, as mentioned in the previous section, consist of a porous and brittle glass core, which is surrounded by a thin layer of coating material. The core material, Poraver®, is produced by heating recycled glass resulting in particles, with diameters ranging from 2 to 4 mm. They have a high porosity of 75.6% (closed pores) and a bulk density of 230 kg/m^3 for grain size between 1 and 2 mm [17]. These properties make them suitable candidates as lightweight filler materials for energy absorption. Since they are manufactured from recycled material, they are environmentally friendly. However, the porous microstructure also makes them brittle. In particular, under dynamic loading, they tend to fragment into finer particles or dust [14]. This leads to a reduction in their energy absorption capability, as well as the formation of dust and increased maintenance requirements. Moreover, they never exist as perfectly spherical objects, resulting in variability in their crushing behaviour and necessitating careful statistical analysis based on different diameter fractions to determine their mechanical response [30]. This is illustrated through the cross section of a coated particle under a laser electron microscope in Fig. 1. The thickness of the continuous layer on the outside varies from 70 to 100 μm. Moreover, the microstructure of the core material is significantly porous.

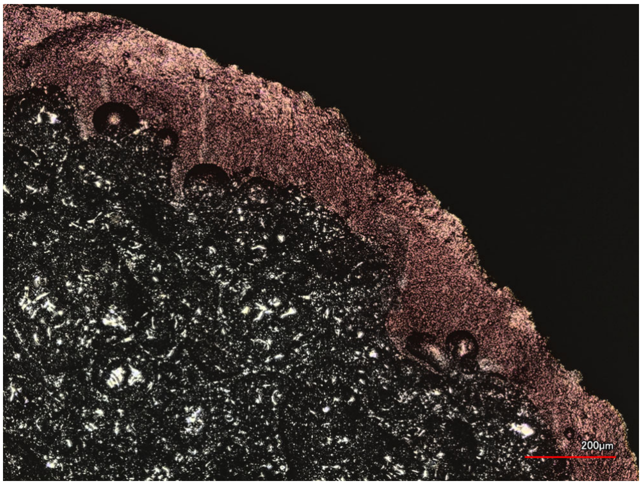

Fig. 1 Cross section of a coated particle under a laser electron microscope, showing a coating thickness of 70–100 μm and the porous structure of the core material Poraver®

3 Experimental setup

To provide calibration and validation data for the numerical model, two types of compression tests were performed, namely the single and multi particle compression tests. These experiments were conducted in a previous study [14], and their key aspects are summarised here.

3.1 Single particle compression test (SPT)

In this experiment, a coated particle is compressed between two flat, rigid steel plates using a Texture Analyzer (Stable Micro Systems Ta.XTplus). The particle is placed on the lower steel base plate, while the upper plate (punch) moves downwards at a constant velocity to crush the particle. The displacement of the punch is recorded together with the applied force. A low compression velocity of 50 μm/s was applied until 35% of strain was reached. This ensures that the loading is slow enough to neglect dynamic effects that might otherwise arise. As mentioned in Sect. 2, due to variability in the particle geometry, the force-displacement curves obtained from such experiments are not identical. Nevertheless, an average curve can be derived and used for calibration and validation purposes. The key metrics for this test include the Young's modulus, crushing force, crushing strain, and energy absorbed. A depiction of the test setup is shown in Fig. 2.

3.2 Multi particle compression test (MPT)

To assess the bulk compressive behaviour of particles, multi particle compression tests were carried out. In this setup, the coated particles were confined within a rigid steel cylinder with an inner diameter d_i of 50 mm. The cylinder was ran-

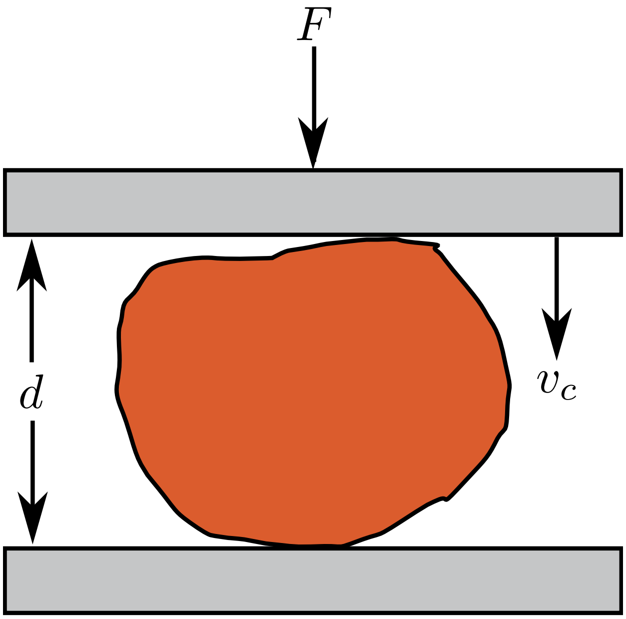

Fig. 2 Experimental setup of a single particle compression test, where d is the particle diameter, v_c is the compression velocity, and F is the force recorded by the punch

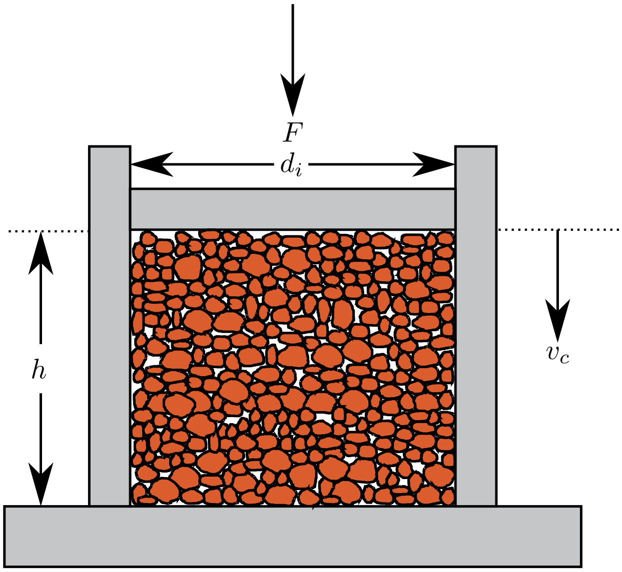

Fig. 3 Experimental setup of a multi particle compression test, where d_i is the inner cylinder diameter, v_c is the compression velocity, h is the height of cylinder, and F is the force recorded by the punch

domly filled with particles such that the mass was 7.1 g. This leads to a variable number of particles per experiment, due to differences in particle size and porosity. Consequently, the total specimen height inside the cylinder also varies. The top surface was levelled to ensure a uniform force distribution across the particle bed. A rigid steel punch was then moved downwards at a constant velocity of 1 mm/min for a total displacement of 11 mm. Note that the velocity is slow enough to make sure dynamic effects are not introduced. A load cell attached to the punch recorded the force during compression. Using this data, stress–strain curves were generated, which were used to determine the energy absorbed, Young's modulus, and to analyse the different phases of the compression process. An illustration of the MPT setup is shown in Fig. 3.

4 Numerical approach

This section details the numerical approach used to simulate the mechanical behaviour of coated particles. DEM is combined with BPM to allow for simulation of the breakage behaviour.

4.1 Discrete element method

The discrete element method is employed to simulate the mechanical interactions of the particles [5, 32]. Each particle is treated as a quasi-rigid body, and the motion is governed by Newton–Euler equations. For a particle p, the translational velocity has to satisfy:

$$m_p \frac{\mathrm{d}\boldsymbol{v}_p}{\mathrm{d}t} = \sum_{i=1}^{n} \boldsymbol{F}_{p,i} + \rho_p V_p \boldsymbol{g}, \tag{1}$$

where m_p is the mass of particle p, $\boldsymbol{v}_p$ is its velocity, $\boldsymbol{F}_{p,i}$ are the contact forces acting on the particle, ρ_p is the mass density of particle, V_p is the volume of particle, $\boldsymbol{g}$ is the gravity, and n is the number of interacting neighbours or contact forces. The rotational motion is described by:

$$I_p \frac{\mathrm{d}\boldsymbol{\omega}_p}{\mathrm{d}t} = \sum_{i=1}^{n} \boldsymbol{M}_{p,i}, \tag{2}$$

where I_p is the moment of inertia of the particle, $\boldsymbol{\omega}_p$ is the angular velocity, and $\boldsymbol{M}_{p,i}$ are the torques acting on the particle. Both equations are solved for each particle p using the leapfrog method [13].

For solving the contact problem, a quasi-rigid sphere DEM approach is implemented, wherein particles are allowed to slightly overlap with each other or with walls. The contact forces are computed as a function of overlap and material properties. We use an elastic contact model with damping known as the Hertz–Mindlin model [11, 26]. The normal contact force is calculated as:

$$\boldsymbol{F}_n = \left(-k_n \xi_n^{3/2} - \eta_n v_{\mathrm{rel},n}\right) \boldsymbol{n}, \tag{3}$$

where ξ_n is the normal overlap (penetration distance), k_n is the normal contact stiffness factor, η_n is the normal damping coefficient, $v_{\text{rel},n}$ is the relative normal velocity, and $\boldsymbol{n}$ is the unit vector in the direction of the contact normal. For Hertzian contact, the stiffness is given by:

$$k_n = \frac{4}{3} E^* \sqrt{R^*}, \tag{4}$$

where E^* is the effective Young's modulus and R^* is the effective radius. The tangential force $\boldsymbol{F}_t$ is calculated using the Mindlin model,

$$\boldsymbol{F}_t = \boldsymbol{F}_t^{\text{prev}} + \Delta \boldsymbol{F}_t + \boldsymbol{F}_{t,\text{damp}}, \tag{5}$$

where $\boldsymbol{F}_t^{\text{prev}}$ is the tangential force from the previous timestep, $\Delta \boldsymbol{F}_t$ is the incremental elastic tangential force, and $\boldsymbol{F}_{t,\text{damp}}$ is the tangential damping force. The incremental elastic tangential force is defined as:

$$\Delta \boldsymbol{F}_t = k_t \Delta \boldsymbol{\xi}_t, \tag{6}$$

where $\Delta \boldsymbol{\xi}_t = \boldsymbol{v}_{\text{rel},t} \Delta t$ is the relative tangential displacement over the time step Δt, and $\boldsymbol{v}_{\text{rel},t}$ is the tangential component of the relative velocity. The tangential stiffness k_t is calculated as:

$$k_t = 8G^* \sqrt{R^* \xi_n}, \tag{7}$$

where G^* is the effective shear modulus. To account for energy dissipation in the tangential direction, a damping force is added:

$$\boldsymbol{F}_{t,\text{damp}} = -\gamma_t \sqrt{k_t M^*} \boldsymbol{v}_{\text{rel},t}, \tag{8}$$

where γ_t is the tangential damping coefficient and M^* is the effective mass. To ensure that the tangential force does not exceed the Coulomb friction limit, it is restricted by:

$$\text{if } |\boldsymbol{F}_t| > \mu_s |\boldsymbol{F}_n|, \quad \boldsymbol{F}_t = \mu_s |\boldsymbol{F}_n| \frac{\boldsymbol{F}_t}{|\boldsymbol{F}_t|}, \tag{9}$$

where μ_s is the sliding friction coefficient. Rolling friction is also considered by introducing a torque that resists the relative rotation of particles. The rolling torque applied to particle i is given by:

$$\boldsymbol{M}_{r,i} = -\mu_r r_i |\boldsymbol{F}_n| \frac{\boldsymbol{\omega}_i}{|\boldsymbol{\omega}_i|}, \tag{10}$$

where μ_r is the rolling friction coefficient, r_i is the radius of particle i, and $\boldsymbol{\omega}_i$ is the angular velocity of the particle. This torque acts against the motion of particles and therefore reduces the tendency to roll freely due to reduction in angular momentum. Moreover, it leads to conversion of kinetic energy into frictional energy. This is important in real granular assemblies where particles experience rolling resistance due to surface roughness, local plastic deformation at the contact point, and viscoelastic effects. Additionally, it can lead to a more static configuration in granular systems where rolling effects are dominated.

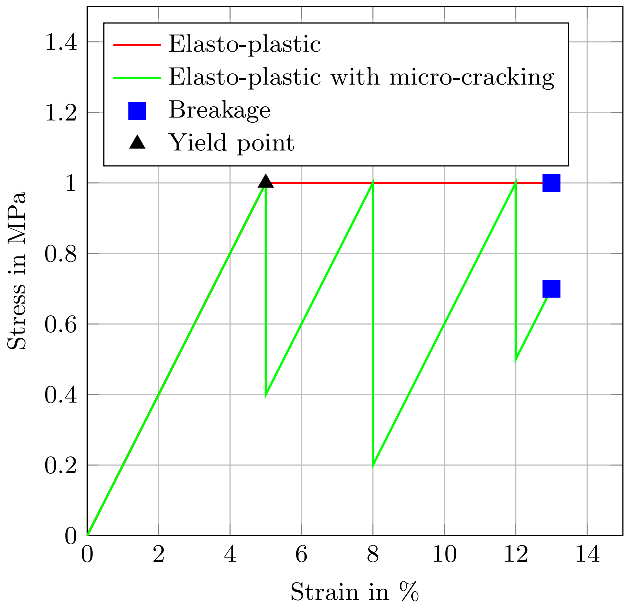

Fig. 4 Comparison of the micro-cracking with the elasto–plastic bond model stress–strain curve

4.2 Bonded particle method

The approach is based on the method introduced by [18] for modelling rock as a cemented assembly of grains. To simulate a coated particle breakage, a single physical coated particle is represented as an agglomerate or cluster of many smaller particles that are bonded or glued to each other. Each bond is virtual as it is massless with its strength and deformability charaterised by the material model along with the geometrical and material parameters. For this work, the model is taken from [22] and depicted in Fig. 4.

The stress in the bond increases linearly with strain until the yield stress is reached. For the elasto–plastic model, once the yield stress $\sigma_{b,y}$ is reached, the stress remains constant during further loading until a critical breakage strain $\varepsilon_{b,\max}$ is exceeded. The bond is then considered broken and removed from the simulation. The total strain in the bond $\varepsilon_{b,T}$ consists of an elastic part $\varepsilon_{b,e}$ and a plastic part $\varepsilon_{b,p}$, such that

$$\varepsilon_{b,T} = \varepsilon_{b,e} + \varepsilon_{b,p}, \tag{11}$$

and the stress in the bond is given by

$$\sigma_b = k_b(\varepsilon_{b,T} - \varepsilon_{b,p}), \tag{12}$$

where k_b is the bond stiffness. The yield condition for the bond is expressed as

$$f(\sigma) = |\sigma_b| - \sigma_{b,y} \leq 0, \tag{13}$$

which limits the maximum stress that can be carried inside the bond and introduces plasticity beyond the yield point. In contrast, the micro-cracking model allows the bond stress to drop when the yield stress is reached, simulating sudden energy releases due to micro-crack formation. Each stress drop is defined probabilistically using a damage factor η_w, uniformly sampled between 0 and 1. The remaining bond stress after a micro-crack is calculated as

$$\sigma_{b,\mathrm{rem}} = \eta_w \sigma_b, \tag{14}$$

and the stress continues to increase linearly again with the same slope as in the elastic region until the yield stress is reached once more. This cycle of yielding, sudden stress drop, and reloading continues until the total strain $\varepsilon_{b,T}$ exceeds the breakage strain $\varepsilon_{b,\max}$, at which point the bond is removed. The purpose of using such a micro-cracking formulation is to account for the experimentally observed crackling and brittle failure mechanisms described in [14]. A full microscopic representation of the porous coating and core structure, as shown earlier in Fig. 1, would require an extremely fine-scale modelling. Instead, this mesoscale approach provides a more computationally feasible method to capture breakage behaviour while maintaining physical realism, as supported by findings in [22].

Regardless of the specific bond model, the underlying computation of stress is rooted in classical beam theory [19]. Each bond is treated like a small elastic beam connecting two particles, and both normal and tangential forces, as well as torques, are computed based on the relative motion between particles. These force and torque increments are updated at every time step and used to determine the evolving stress state inside the bond. The incremental bond forces and moments are given by:

$$\Delta \boldsymbol{F}_{b,n} = \frac{E_b}{L_b} A_b \boldsymbol{v}_{\mathrm{rel},n} \Delta t, \tag{15}$$

$$\Delta \boldsymbol{F}_{b,t} = \frac{E_b}{2L_b(1+\nu)} A_b \boldsymbol{v}_{\mathrm{rel},t} \Delta t, \tag{16}$$

$$\Delta \boldsymbol{M}_{b,n} = -\frac{E_b}{2L_b(1+\nu)} J_b \boldsymbol{\omega}_{\mathrm{rel},n} \Delta t, \tag{17}$$

$$\Delta \boldsymbol{M}_{b,t} = -\frac{E_b}{L_b} I_b \boldsymbol{\omega}_{\mathrm{rel},t} \Delta t, \tag{18}$$

where E_b is the bond's Young's modulus, L_b is its length, A_b is the cross-sectional area, and ν is the Poisson's ratio. The terms $\boldsymbol{v}_{\mathrm{rel},n}$ and $\boldsymbol{v}_{\mathrm{rel},t}$ denote the normal and tangential components of the relative translational velocity, while $\boldsymbol{\omega}_{\mathrm{rel},n}$ and $\boldsymbol{\omega}_{\mathrm{rel},t}$ represent the relative rotational velocity components. The geometric terms I_b and J_b are the moment of inertia and polar moment of inertia of the bond's cross section. Once these force and torque increments are determined, the resulting bond stresses can be computed as:

$$\sigma_{b,n} = \frac{|\boldsymbol{F}_{b,n}|}{A_b} + \frac{|\boldsymbol{M}_{b,t}|}{I_b} R_b, \tag{19}$$

$$\tau_{b,t} = \frac{|\boldsymbol{F}_{b,t}|}{A_b} + \frac{|\boldsymbol{M}_{b,n}|}{J_b} R_b, \tag{20}$$

where R_b is the bond radius. These stress measures are then compared against model-specific strength criteria to determine if the bond fails. In this way, beam theory provides a consistent foundation for all bond formulations, whether purely elastic or incorporating complex fracture mechanisms such as plasticity and micro-cracking.

4.3 High- and low-fidelity approach

As mentioned in Sect. 1, we use the open-source code MUSEN [6] to simulate particle breakage using the DEM and BPM approaches described in the previous section. However, such an approach is computationally expensive. Firstly, depending on the number of particles, the degrees of freedom increase significantly, especially if one attempts to model the microstructure of the coated particle illustrated in Fig. 1. This would require reducing the diameter of DEM particles to below a nanometre, which, when combined with BPM, would necessitate a large number of particles to represent a single physical particle. Additionally, large-scale experiments would become computationally infeasible.

To overcome this, the model was simplified at the mesoscale level rather than at the microscale, allowing for reasonable fidelity while reducing computational cost. Secondly, significant memory is required at each time step to keep track of contact partners. MUSEN addresses this using Verlet lists [27], which are combined with the linked-cell algorithm [21] to reduce computational time through parallelisation. However, even this optimisation is insufficient for large-scale multi particle simulations, where the particle count may exceed one million. Furthermore, the number of contact partners can increase significantly in highly compressed regions. To further simplify the approach, two different numerical models were developed, both depicted in Fig. 5.

For both setups, the overall geometry of the model is spherical. This ensures that the stress–strain relationships presented in latter sections are independent of the agglomerate shape. Instead, the results highlight how both high- (HF) and low-fidelity (LF) approaches can be used within the same setup to achieve similar outcomes. This is consistent with the findings of [22], where variations in porosity and the

Fig. 5 Cross-section of the DEM-BPM representation of a coated particle


(a) Low-fidelity

(b) High-fidelity

Table 1 Summary of the differences in structure between the high- and low-fidelity model

	HF	LF	Factor of reduction
Parameters	28	14	2.00
Bonds	8685	3180	2.73
Particles	2141	484	4.42

geometry used for particle generation significantly affected the stress–strain response during compression tests. Once the agglomerate geometry is fixed, the difference between LF and HF models lies in the representation of the coating layer. As shown earlier in Fig. 1, the dense coating layer is approximately 100 µm thick. To model this, a significant number of smaller particles (diameter 0.1 mm, shown in dark orange) are required around the core cluster of Poraver particles (diameter 0.25 mm, shown in dark yellow), as seen in Fig. 5. Additionally, bonds are modelled between coating-coating as well as between Poraver®-coating particles (light orange). The bonds between Poraver®-Poraver® particles are illustrated in light yellow. In contrast, the low-fidelity model fills the space around the core with only Poraver® particles. The smaller coating particles and bonds are neglected. The diameter of these core particles remains unchanged. Consequently, the number of parameters to calibrate, the number of bonds, and the number of particles are reduced by factors of 2.00 ×, 2.73 ×, and 4.42 ×, respectively. These reductions are summarised in Table 1.

5 Parameter identification

In order to predict the results of the single and multi particle compression tests using the numerical model, the parameters that significantly affect the outcome are identified and optimised. These include both structural and material parameters. Many of these parameters are not physically measurable, such as the bond length, since no equivalent quantity exists in the real microstructure shown in Fig. 1, and their influence on the model output can be complex and coupled. Therefore, we employ a two-step identification process: first, a sensitivity analysis is conducted to determine which parameters significantly affect the outcome of interest, followed by an optimisation algorithm, in this case particle swarm optimisation (PSO), to fine-tune the parameters for best agreement with experimental data. This strategy aligns with previous studies in DEM calibration, where sensitivity analysis is used to filter parameters [8], followed by optimisation [16, 28]. Note that parameter identification is performed using the single particle compression test due to the significantly higher computational cost of the multi particle simulations, as described in Sect. 6.2.

5.1 Sensitivity analysis

As mentioned in the previous section, the parameters can be divided into two main groups. The first group, known as the structural parameters, is listed in Table 2. These are kept fixed for both HF and LF models, as described in Sect. 4.3. Although they do influence the force-displacement response obtained from compression simulations, refer to [22], they are held constant under the assumption that a fixed spherical numerical model is considered with reasonable particle and bond density. This provides reasonable force-displacement curves seen later in Sect. 6.1. Note that bonds exist both between coating particles, referred to as coating-coating, and between coating and Poraver® particles, referred to as Poraver®-coating. To reduce the number of parameters and simplify the model, identical parameters are used for both bond types. Therefore, these two bonds are henceforth referred to collectively as Poraver®-coating-coating.

The second group comprises the material parameters, illustrated in Fig. 6. These include the parameters introduced due to the coating layer around the core agglomerate. The sensitivity analysis is conducted using the single particle compression test described in Sect. 3.1. This test setup allows identification of the crushing point of the agglomerate, from which the crushing force and displacement are extracted.

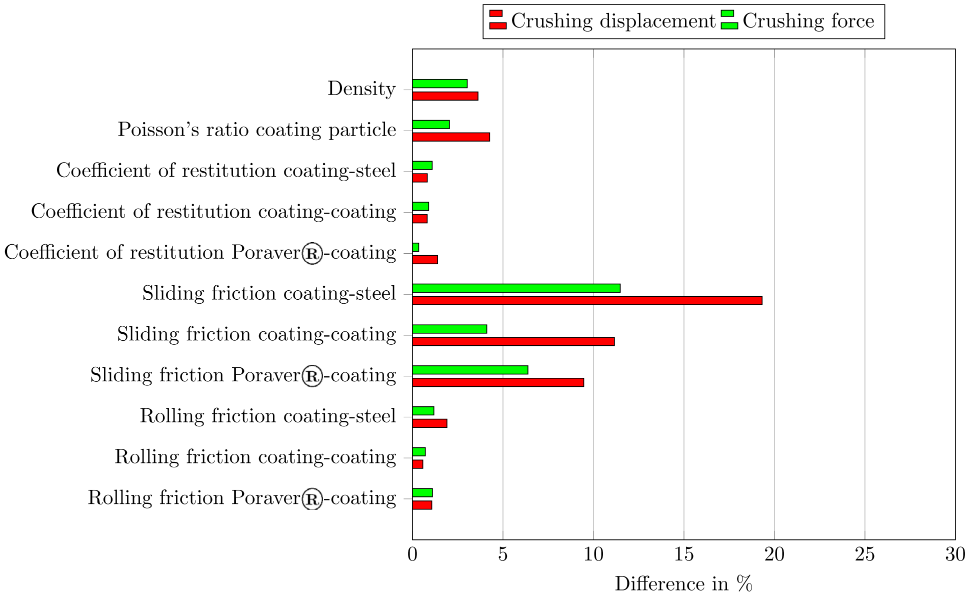

Fig. 6 Material input parameters

Table 2 Structural input parameters

Parameter	Value
Particle diameter in mm	
Coating	0.1
Poraver®	0.25
Porosity	
Coating	0.5
Poraver®	0.36
Bond diameter in mm	
Poraver®-coating-coating	0.1
Poraver®-Poraver®	0.25
Minimum bond overlap in mm	
Poraver®-coating-coating	−0.05
Poraver®-Poraver®	−0.125
Maximum bond overlap in mm	
Poraver®-coating-coating	0.05
Poraver®-Poraver®	0.125

During the analysis, each parameter listed in Fig. 6 is perturbed by a factor of 10, and the resulting crushing force and displacement are recorded. This perturbation factor is based on the findings of [22], where a similar parameter study was conducted for the core material. There, varying parameters by a factor of 10 led to significant changes in the simulation results.

It is observed that three parameters show at least a 5% influence on the results, namely all the sliding friction coefficients. This is expected, as sliding friction affects the tangential force $\boldsymbol{F}_t$ in the Hertz–Mindlin contact model, which in turn contributes to the total force $\boldsymbol{F}$. In addition, four more parameters bring the total number of sensitive parameters to seven. These include the Young's modulus, which influences the bond stiffness k_b, used to compute the elastic stress σ_b, and the breakage strains of Poraver®-coating-coating and Poraver®-Poraver® bonds. These parameters are included regardless of their statistical sensitivity for two reasons: first, they directly affect the calculation of stress–strain behaviour within the bond model; and second, as highlighted in [22], they exert a significant influence on the resulting crushing stress and strain.

By narrowing the focus to the most sensitive parameters, the dimensionality of the optimisation problem is reduced. The less influential parameters are fixed and are listed in Table 3. The parameters for the core structure, Poraver®, are adopted from [14, 22, 29]. The density of the coating is taken from [12], while the Poisson's ratio is approximated using values reported for paraffin wax, as found in [31]. Note that the densities for both coating and Poraver® have been increased due to mass scaling, see Sect. 6. The coefficients of restitution and rolling friction are conservatively set to 0.1, under the assumption that these parameters primarily influence the dynamic behaviour of the simulation. Since the simulations are intended to be quasi-static, their effect is expected to be limited to the convergence of the numerical solution. Additionally, while the yield strength of the wax bonds was not part of the formal optimisation routine, an initial set of trial simulations led to the identification of a value around 6 MPa. This value consistently produced force-displacement curves that qualitatively matched experimental observations. Therefore, it was retained as a fixed parameter for the remainder of the study.

For the LF model, parameters for the coating are absent because the smaller particles are not explicitly modelled.

Table 3 Fixed material input parameters

Parameter	Value
Density in kg/m^3	
Coating	96,000
Poraver®	79,239.5
Poisson's ratio	
Coating	0.37
Poraver®	0.30
Coefficient of restitution	
Coating-steel	0.1
Coating-coating	0.1
Poraver®-coating	0.1
Poraver®-steel	0.1
Poraver®-Poraver®	0.1
Rolling friction	
Coating-steel	0.1
Coating-coating	0.1
Poraver®-coating	0.1
Poraver®-steel	0.1
Poraver®-Poraver®	0.1
Sliding friction	
Poraver®-steel	0.48
Poraver®-Poraver®	0.87
Yield strength in MPa	
Poraver®-coating-coating bonds	6
Poraver®-Poraver® bonds	2.5

Therefore, their effect is incorporated by varying the Young's modulus and breakage strain of the core in the latter section.

5.2 Particle swarm optimisation

To optimise the identified sensitive parameters, we use the particle swarm algorithm, proposed by [9]. In this algorithm, the positions and velocities of particles are updated based on both individual and global best solutions. PSO is well suited here because our objective function, the error between simulation and experimental results, does not have an analytical gradient, and each function evaluation requires a full DEM simulation. We define the objective function $J(\boldsymbol{p})$ as the least-squares error between the simulation and experimental force-displacement curves for the single particle compression test:

$$J(\boldsymbol{p}) = \sum_{i=1}^{n} \left[F_{\text{sim}}(x_i; \boldsymbol{p}) - F_{\text{exp}}(x_i)\right]^2 \tag{21}$$

where $F_{\text{sim}}(x_i; \boldsymbol{p})$ is the simulated force at displacement x_i using parameter set $\boldsymbol{p}$, $F_{\text{exp}}(x_i)$ is the corresponding experimental force, and n is the number of displacement points. The averaged experimental reference curve is the red plot shown in Fig. 7.

The optimisation was implemented using the MATLAB Optimisation Toolbox [25]. Initial positions were randomly generated within the search bounds. The upper and lower bounds with the final optimised values are presented in Table 4 for HF and LF models.

These bounds were chosen based on physical reasoning and prior trials to ensure that the optimum lies within the defined search space. This is demonstrated using two different high-fidelity models, HF-A and HF-B, presented in Table 4. In HF-A, the coating material exhibits a higher Young's modulus and a lower breakage strain compared to the core material. Combined with elevated friction coefficients, this configuration captures the brittle fracture behaviour and sticking effects observed experimentally [14]. In contrast, HF-B employs an inverse setup, where the core material has a higher Young's modulus and a lower breakage strain than the coating. The resulting effects are further discussed in Sect. 6. Moreover, the low-fidelity model does not include explicit coating particles, and therefore, does not consider sliding friction. Instead, it is calibrated solely based on total energy absorption. Consequently, the LF model is limited in its ability to simulate frictional interactions in coated particle systems.

6 Simulation and validation

This section presents the results of the DEM-BPM approach with parameter identification performed through sensitivity analysis and the particle swarm optimisation algorithm. The single particle compression test is used for calibration, followed by the multi particle compression test for validation. A comparison between high- and low-fidelity models is also conducted to highlight differences in accuracy and performance. To simulate these tests, a quasi-static simulation setup is devised. The time step is fixed at 5×10^{-8} s, which is smaller than the recommended critical time step. The recommended critical value is defined as 10% of the minimum between the Rayleigh time step size Δ_{Rayleigh} and the bond time step size Δ_{bond} [1, 15]. Additionally, mass scaling by a factor of 100 is applied to reduce the critical time step size. The particle density and gravitational acceleration, as listed in Table 3, are adjusted accordingly. This scaling factor remains within acceptable bounds as demonstrated in [22]. The compression velocity v_c is set to 10 mm/s for the SPT and 100 mm/s for the MPT. With this configuration, the simulations can be conducted within feasible computational times without compromising accuracy.

Table 4 Optimised parameter sets for HF and LF models

Parameter	HF-A		HF-B		LF	
	Value	Search domain	Value	Search domain	Value	Search domain
Sliding friction						
Coating-coating	0.5273	[0.5−0.9]	0.5008	[0.5−0.9]	–	–
Coating-steel	0.8306	[0.5−0.9]	0.8796	[0.5−0.9]	–	–
Poraver®-coating	0.9000	[0.5−0.9]	0.7924	[0.5−0.9]	–	–
Young's modulus in MPa						
Coating bonds and particles	2441	[1e+9-9e+9]	690	[1e+8-1e+9]	–	–
Poraver® bonds and particles	861	[1e+8-1e+9]	993	[1e+8-1e+9]	502	[1e+8-1e+10]
Breakage strain						
Poraver®-Coating-coating bonds	0.0026	[1e-4-5e-3]	0.098795	[1e-5-1e-1]	–	–
Poraver®-Poraver® bonds	0.0050	[5e-3-1e-1]	0.00005	[1e-5-1e-1]	0.0033	[1e-5-1e-2]

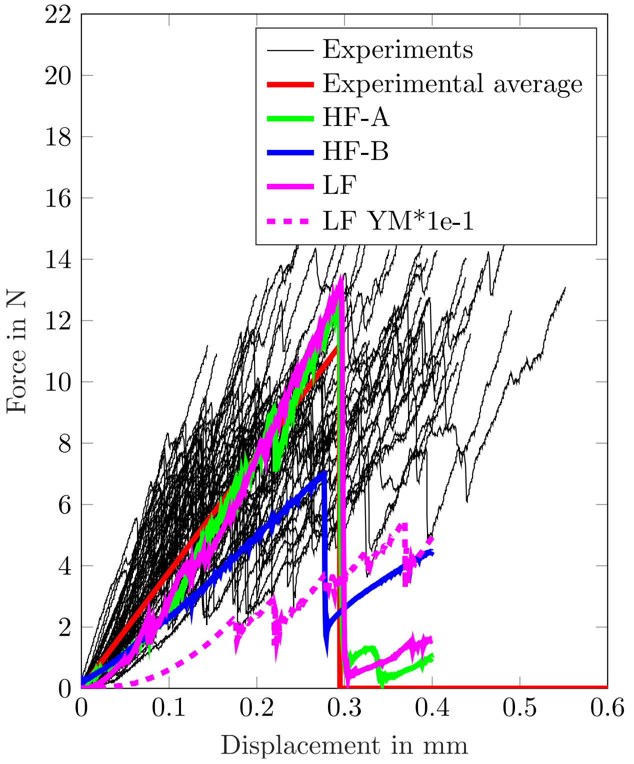

Fig. 7 Force-displacement curve of SPT for experimental diameter fraction 2.0-2.5 mm showing the experimental average, and HF and LF model results

6.1 Compression tests

The test setup has been described previously in Sect. 3. The force-displacement results are illustrated in Fig. 7 for the experimental diameter fraction 2.0−2.5 mm.

The experimental plots in black depict the variability in the experimental results. As discussed in Sect. 2, no two particles have the same microstructure or shape. Furthermore, the force-displacement relationship is highly nonlinear. Nevertheless, an average curve, highlighted with a thick red line, is generated. This curve begins at the origin and increases linearly until the breakage force and crushing displacement of 11.18 N and 0.294 mm, respectively, are reached. Beyond this point, the force drops to zero and remains constant. As mentioned earlier, this average curve is used in the objective function to optimise parameters for both the HF and LF models. The results are depicted in green, blue and magenta, respectively.

Except for the HF-B model, the optimised parameter sets for both models show good agreement with the average curve. The force increases in a nonlinear fashion. The bond model described in Sect. 4.2 enables micro-cracking behaviour, similar to that observed in the experiments. This is achieved through bond breakage, which causes a drop in force followed by a rise. At a breakage displacement of 0.3 mm, a significant number of bonds fail, leading to the complete crushing of the agglomerate.

Notably, the LF model uses fewer parameters, particles, and bonds, but still manages to capture the same compressive overall behaviour as the HF-A model. Nevertheless, small differences exist. The maximum force predicted by both models is around 13 N, with a difference of 1.82 N. Additionally, the initial stiffness of the numerical models is lower than that of the experimental average. The HF-A model performs slightly better in this respect, matching the stiffness of the red curve up to 0.05 mm. This is explained by the presence of stiffer coating particles in the HF model. As the coating layer breaks, the steel punch travels a short distance before the core structure begins to resist compression. In the LF model, these stiffer particles are absent, so it cannot provide as much initial resistance. Furthermore, the optimisation algorithm compensates for the initial discrepancy by increasing the breakage force so that the overall energy absorbed remains similar.

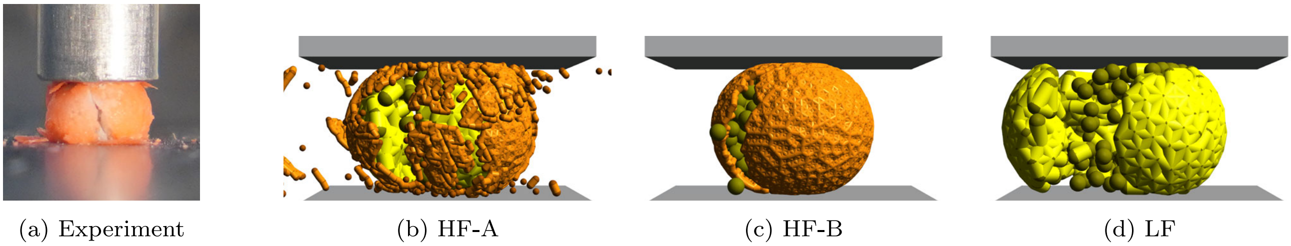
(a) Experiment (b) HF-A (c) HF-B (d) LF

Fig. 8 Comparison of particle breakage in the single particle compression test between experiment and numerical models

The HF-B model produces the least accurate result among the three configurations. As discussed earlier in Sect. 5.2, the lower Young's modulus and higher breakage strain lead to insufficient bond breakage between the coating particles. Consequently, the slope of the force-displacement curve is reduced. Additionally, the extent of microcracking is lower compared to other models, as indicated by the smoother force-displacement response. In fact, the bonds between the core particles tend to break earlier. This behaviour is illustrated in Fig. 8, where all models are compared during compression alongside an image from the physical experiment. In the case of HF-A, the coating fractures significantly during the breakage of agglomerate. In contrast, HF-B shows an intact coating while the core structure fails. In the experiment, some of the coating material along with Poraver® breaks initially; however, most of it remains intact. The third model, LF, does not explicitly model the coating and can only reproduce the overall breakage of the physical particle.

Despite these differences, both the HF and LF results fall within the experimental spread and can therefore be used to validate the multi particle compression test described next. With the optimised agglomerates from the HF and LF approaches, we evaluate their suitability against the multi particle compression test experiments.

The largest difference between the HF and LF approaches is observed in this simulation, where an attempt was made to model the same number of agglomerates as the physical particles in the cylinder, i.e. an average of 2306 particles. However, the GPU memory (Nvidia GeForce RTX 3090 with 24 GB of GDDR6X) was insufficient, and the simulation was unable to run. As described in Sect. 4.3, the Verlet list stores all contact interactions between particles. When the database becomes too large, it causes the simulation to crash. Nevertheless, the model was tested with 1300 agglomerates, more than 50% of the physical particle count, and its suitability was verified. To ensure comparability, both experimental and simulation stress–strain curves were normalised. The original experiment was conducted using a cylinder with an average height *h* of 14.3 mm, as shown in Fig. 3. Due to the reduced number of agglomerates, a portion of the punch displacement is lost before any significant reaction force is observed. Therefore, a threshold force of 1 kN was selected to initiate strain calculation. This ensures that the strain, set to zero, begins at the point where the punch registers at least 1 kN of force. Furthermore, this approach minimises initial noise in the experiments arising from particle rearrangement during initial contact with the punch and allows for a more uniform stress increase, starting from an initial value of approximately 0.5 MPa. Overall, this normalisation strategy enables a more consistent comparison between simulations and experiments, despite differences in the number of agglomerates and physical particles.

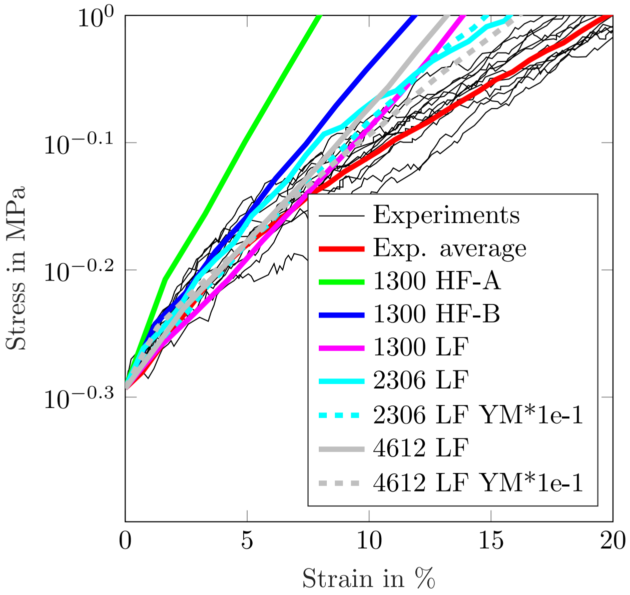

Fig. 9 Stress–strain results of MPT comparing experimental average, HF and LF model results up to strain 20%

As before, the black lines represent the experimental results for different diameter fractions, filtered through various particle shapes, see [14]. Although particles of varying diameters are present, the variability is lower than in SPT. This suggests that scaling up the experiment, where the average number of particles inside the cylinder was 2306, leads to reduced inhomogeneity between particles. This supports the decision to fix the agglomerate shape, as discussed in Sect. 5. Although using agglomerates with different shapes and structures would increase model fidelity, it would also

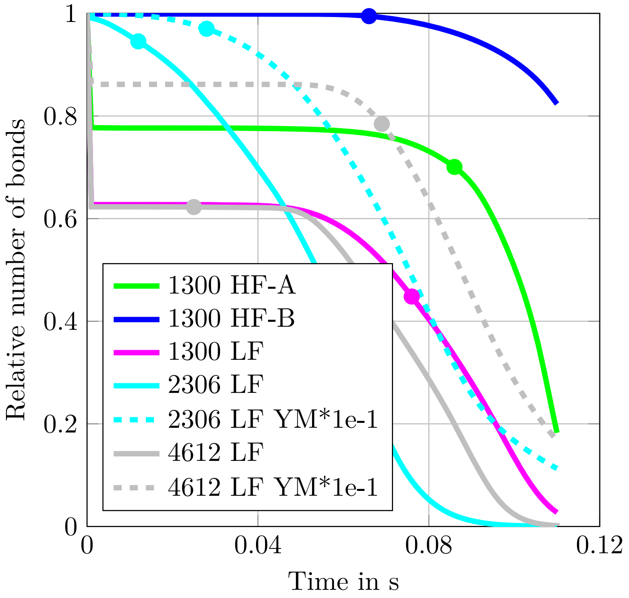

Fig. 10 Change in relative number of bonds during the simulation

require repeating the optimisation process multiple times with only marginal gains in accuracy. A trade-off must be made between fidelity and computational cost. Nevertheless, the current comparison still provides insight into these trade-offs.

We begin by examining the stress–strain results up to 20% strain in Fig. 9. As observed previously in the SPT, the HF-A model (green) exhibits higher stiffness compared to the other simulations due to the presence of stiffer coating particles on the exterior. Moreover, a significant portion of bonds break early in the simulation, before the threshold force is even reached, as shown in Fig. 10. The relative number of bonds refers to change in the number of bonds, divided by the initial total number of bonds in the system. The circular marker indicates the point at which the reaction force reaches the threshold and the strain is reset to 0%. As mentioned earlier, 20% of the bonds are lost before the threshold-based force calculation from the threshold even begins. In contrast, the HF-B model, although stiffer than the experimental results, produces a lower stiffness than HF-A. While both HF-A and HF-B start with the same number of bonds, HF-A experiences a more significant reduction in bond count. While the number of bonds does continue to decrease after the initialisation point, the reduction is insufficient to dissipate the compressive energy effectively. This indicates that although HF-A showed promise in the SPT, its applicability to larger-scale compression tests is uncertain.

For a fair comparison, the LF simulation (magenta) is performed with 1300 agglomerates. Its stiffness is lower than both HF-A and HF-B but still exceeds the experimental average. This indicates that lack of stiffer coating particles did not contribute to increased stress response. Nevertheless, almost 40% of bonds are broken before the initialisation, leading to lack of energy dissipation as before with HF models. Interestingly, increasing the number of LF agglomerates to 2306 (cyan) yields a better agreement with the experimental results. This can be attributed to the presence of additional bonds, more than 90%, compared to the previous setups, once the threshold force is reached. Moreover, to fit the same number of agglomerates as in the physical experiments, pre-compression is introduced due to the simulation setup. The total cylinder height is fixed at 14 mm; thus, when 2306 agglomerates are generated, space becomes insufficient. Consequently, some particles overlap significantly even before the compression begins, resulting in pre-stressed bonds. Once the simulation starts and breakage is enabled, bonds fail more rapidly. This behaviour is evident from the steeper decline in bond count after the magenta marker in Fig. 10. Moreover, the threshold force is reached sooner.

To investigate further, another LF model is generated with 4612 agglomerates (grey). In this case, fitting all particles within the original 14 mm cylinder height is impractical, therefore it is increased to 41 mm to prevent notable pre-compression and overlapping. The results are shown in both Figs. 9 and 10. As in the 1300 agglomerate setup, the threshold force is reached later with almost 40% loss in bond count. Furthermore, the slope of the stress–strain curve does not decrease upon reaching the threshold, since the number of bonds in the system remains stable, see the grey marker in Fig. 4, indicating the absence of pre-compression effects. This indicates that up to 20% compressive strain, most of original structure should remain intact, specifically at least 85% of the bonds. This can be achieved either by increasing the number of agglomerates in the system (although this introduces pre-compression, as seen in the case of 2600 LF), or by ensuring that the bond count does not change significantly before reaching the threshold, as in the case of HF-B.

For the same test, the results for large strain up to 70% are depicted in Fig. 11. All setups without pre-compression, 1300 agglomerates for both HF and LF, and 4612 LF, begin to exhibit a significant increase in stress after 20% strain. In addition to the lack of initial bond count, they are not breaking down quickly enough to compensate for the increasing overlap between particles. This is illustrated in Fig. 12, which shows the relative overlap calculated by dividing the average overlap of all particles by the largest particle diameter, 0.25 mm.

According to the assumptions of the Hertz–Mindlin contact theory, the normal overlap ξ_n between particles should remain small to ensure accurate contact force calculations. A widely accepted guideline is that the overlap should not exceed 1–2% of the particle radius, or equivalently, 2–4% of the particle diameter [11, 26]. Apart from the HF models, the other setups show particle–particle overlap exceeding the

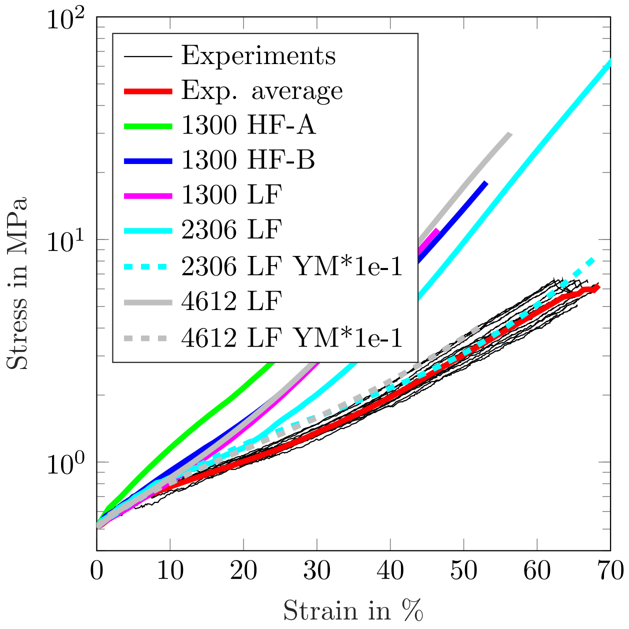

Fig. 11 Stress–strain results of MPT comparing experimental average, HF and LF model results up to strain 70%

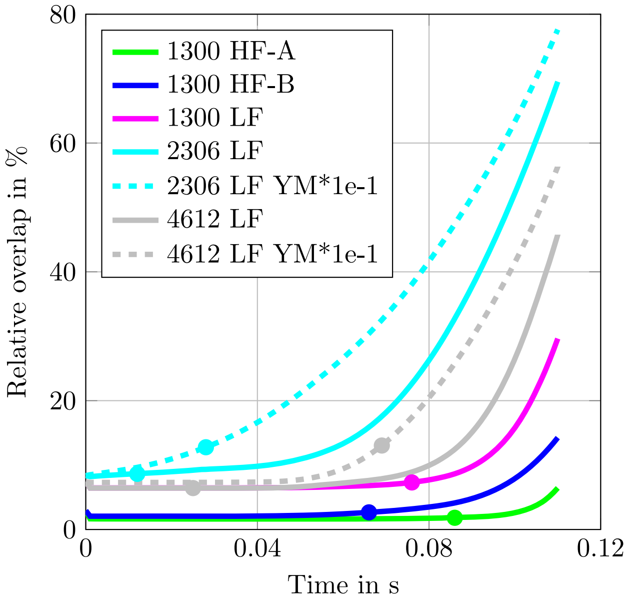

Fig. 12 Change in relative overlap during the simulation

recommended value, which can result in a rapid increase in stress relative to the rate of bond breakage.

To reduce this effect, we rerun both the LF model with 2306 and 4612 agglomerates using a lower Young's modulus, reduced by an order of magnitude 10. The results are represented by the dashed lines in Fig. 11, with 2306 LF YM*1e-1 and 4612 LF YM*1e-1 in magenta and grey, respectively. Lowering the Young's modulus increases the overlap, see Fig. 12, but reduces the normal force $\boldsymbol{F}_n$ calculated using the Hertz-Mindlin contact model. As a result, lower stresses are generated due to softer contact interactions, as observed in Fig. 11. These simulation results lie closer to the experimental curves, particularly in the large strain region where significant compaction is expected. A similar approach is used for modelling fracture in agglomerates via contact mechanics in [7]. To observe its effect in SPT, LF YM*1e-1 (dashed magenta) is depicted in Fig. 7. As expected, the slope of force-displacement decreases and deviates from the averaged experimental result.

Overall, these observations suggest that while the SPT results provide valuable quantitative and qualitative insights into the behaviour of single particles, they cannot be directly applied to larger compression problems. The presence of a coating layer on the exterior does not offer a significant advantage in the bulk compressive response; instead, it considerably increases the computational cost, making the simulation of larger systems infeasible. Moreover, the inclusion of stiffer particles can result in elevated stresses, causing bond breakage even before the threshold force in the simulation is reached. On the other hand, in the LF model, even with a larger number of agglomerates, the rate of bond breakage is not sufficient to keep pace with the increasing overlap at contact points. One way to compensate for this is to precompress the agglomerate such that the threshold force is reached earlier and more bonds are broken. Nevertheless, the parameters identified through the SPT must be further finetuned and validated using MPT before they can be reliably applied to large-scale simulations.

6.2 Computational times

As noted earlier in Table 1, the HF and LF approaches differ in the number of parameters, bonds, and particles. This results in varying computational times for SPT and MPT, shown in Figs. 13 and 14, respectively. Simulations were performed on a GPU using Nvidia GeForce RTX 3090 with 24 GB GDDR6X memory and 10496 CUDA cores.

In the case of SPT, the LF model was solved 1.4 × faster than the HF model. For MPT, the speed-up was by a factor of 3.3. This is expected, as the LF model has fewer degrees of freedom and a smaller database that stores interactions between particles. While it is not possible to derive an exact equation for the computational time of a given setup, it can be stated with reasonable confidence that the LF model significantly reduces computational effort. As the number of agglomerates increases, the relative speed-up grows, suggesting that the LF model is promising for large-scale simulations.

6.3 Uncoated particles

This section adds a further layer of validation for testing the two-step methodology for the identification of param-

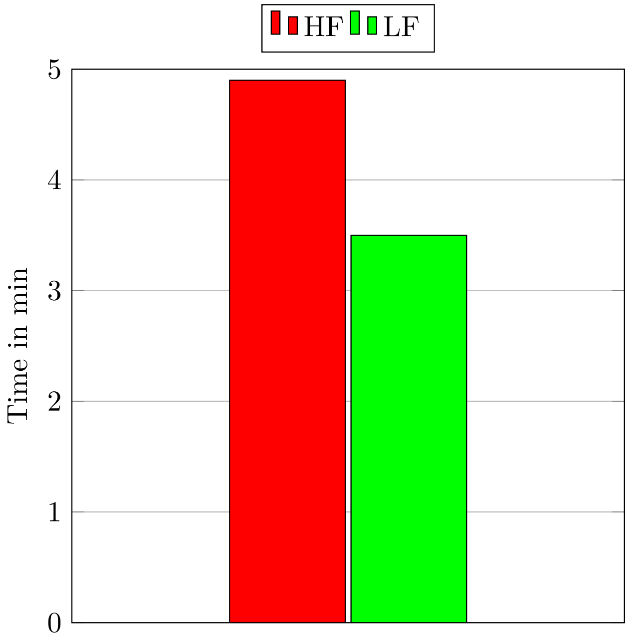

Fig. 13 Computational times for low- and high-fidelity DEM models for single particle compression

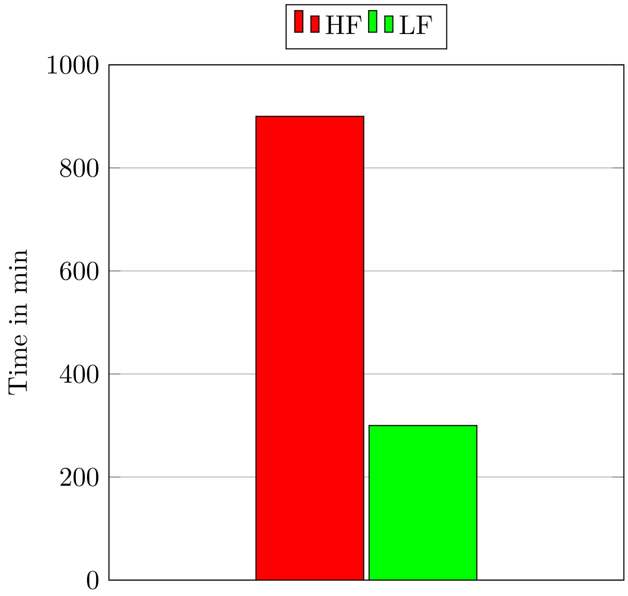

Fig. 14 Computational times for low- and high-fidelity DEM models for multiple particle compression

eters mentioned in the previous sections. For this purpose, we examine the breakage of uncoated particles. The key structural difference lies in the absence of the coating layer. Therefore, the microstructure consists only of Poraver®. In comparison to Fig. 1, only the core structure exists; the thin coating layer is non-existent. The core structure thus consists solely of porous Poraver®.

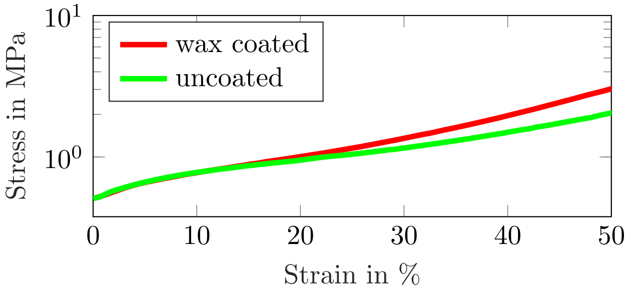

Fig. 15 Stress–strain results of MPT comparing experimental average of wax coated and uncoated Poraver® particles

To highlight the differences between the coated and uncoated particles in terms of energy absorption for applications in large-scale compression experiments, the stress–strain response from the multi particle compression experiments is shown in Fig. 15.

Both the wax coated and uncoated particles show a similar stress–strain response up to 15% strain. As the compression increases, the stress in the coated particles rises more than in the uncoated particles. This indicates that the energy absorbed by the coated particles, represented by the area under the stress–strain curve, is greater than that of the uncoated particles. This characteristic is advantageous, as noted earlier in Sect. 1, for applications where energy absorption during compression is important.

The numerical model is similar to the low-fidelity model illustrated in Fig. 5. Since the coating layer does not exist, the LF model effectively becomes a high-fidelity model, as no physical aspect of the particle is neglected. Although the exact microstructure is not built using CT scans, approximations are made via a mesoscale approach. To follow a similar procedure as with the coated particles, an average diameter of 2.16 mm from the diameter fraction 2.0−2.5 mm is used [14]. Given the size difference compared to coated particles, the number of bonds and particles in the agglomerate are 2665 and 412, respectively. As mentioned earlier, this is quantitatively similar to the LF model, see Table 1. Additionally, the structural parameters of the core structure in a coated particle, i.e. between Poraver®-Poraver® as shown in Table 2, are kept constant. The remaining parameters are optimised, similar to the coated particles, using the particle swarm algorithm on the average experimental force-displacement curve from the single particle compression test. These are listed in Table 5 and illustrated in Fig. 16. Note that the setup for compression tests is same as that of the coated particles, except for the simulation time step in MPT which is set to 5×10^{-7} s.

The black lines represent the experiments. Note that not all compression test results are plotted to improve visibility. More information is available in [30]. As before, each physical particle compression yields a unique force-displacement curve. The force also decreases at different displacement val-

Table 5 Optimised parameter set for the uncoated Poraver® particle numerical model

Parameter	Value	Search domain
Sliding friction		
Poraver®-steel	0.7212	[0.5−0.9]
Poraver®-Poraver®	0.7518	[0.5−0.9]
Young's modulus in MPa		
Poraver® bonds and particles	400	[1e8–1e9]
Breakage strain		
Poraver®-Poraver® bonds	0.0045	[1e-5–1e-2]
Yield stress in MPa		
Poraver®-Poraver® bonds	9.2	[5e+5–1e+7]

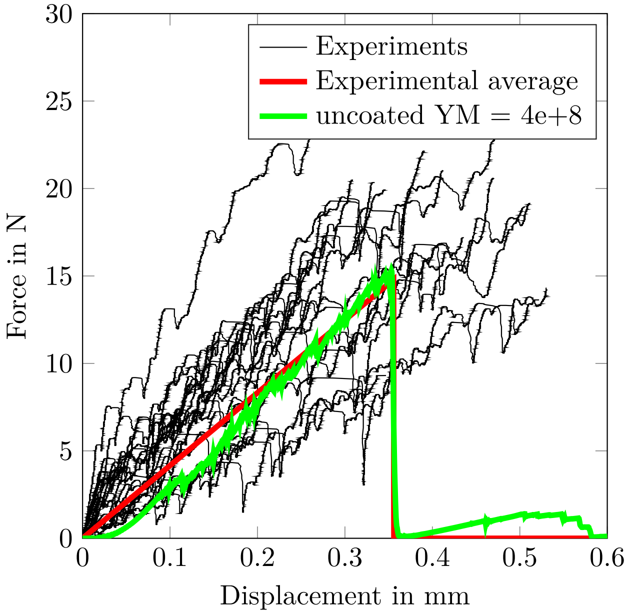

Fig. 16 Force-displacement curve of SPT for experimental diameter fraction 2.0−2.5 mm of uncoated Poraver® particles showing the experimental average and numerical results

ues due to micro-cracking. Similar to the coated particles, the use of an elasto–plastic micro-cracking bond model helps to simulate this behaviour, as shown by the dips in force in the green plot. This enables representation of microcracks and energy dissipation before most bonds in the agglomerate are broken. As mentioned earlier, the simulation curve is optimised around the average experimental curve in red, with a breakage force and displacement of 14.81 N and 0.356 mm, respectively. The numerical model provides a reasonably accurate force-displacement response. More importantly, it lies within the experimental distribution.

To test the accuracy of the optimised agglomerate, the multi particle compression test is carried out. For the 2.0–2.5 mm diameter fraction in the experiments, an average of 3127 physical particles was present. Accordingly, the same number of agglomerates was randomly generated inside the cylinder. Since the uncoated particles are smaller than the coated ones, more particles are needed for the same overall mass. Because the smaller particles used to model the coating in the high-fidelity HF-A and HF-B models do not exist here, the same number of agglomerates as physical particles can be generated. The results of the compression tests are shown in Fig. 17.

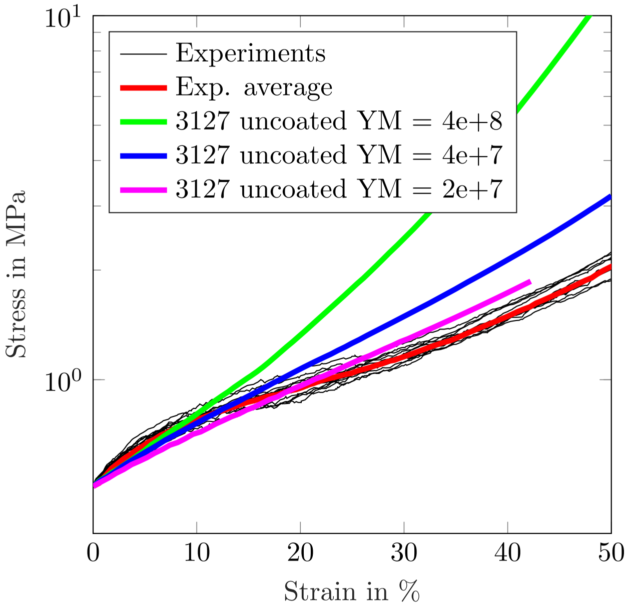

Fig. 17 Stress–strain results of uncoated MPT comparing experimental average and numerical results up to strain 50%

The black lines represent the experiments. As with the coated particles, the distribution of compression results narrows as particle count increases. Nevertheless, an average curve is extracted (in red). The optimised agglomerate results are shown in green. As before, the results lie within the experimental distribution up to 10% strain. Beyond this, the simulated stress increases rapidly. As previously explained in Sect. 6.1 for the MPT, the stress–strain values are normalised. This means that the point at which the force recorded by the punch reaches 1 kN is where the strain calculation starts, i.e. strain is set to zero at that point. As a result, any displacement occurring before this threshold is not captured. Additionally, the number of bonds begins to decrease even before the 1 kN stress threshold is reached, while the strain is reset to zero, as shown in Fig. 18. As a result, fewer bonds are available to dissipate energy via breakage. To improve the match with experimental results, the Young's modulus of the particles is reduced by a factor 10. At the start of the simulation, the relative overlap for the optimised agglomerate (green) is about 9%, more than twice the recommended value, see Fig. 19. Reducing the Young's modulus increases the overlap but also softens the contact. To further improve agreement with

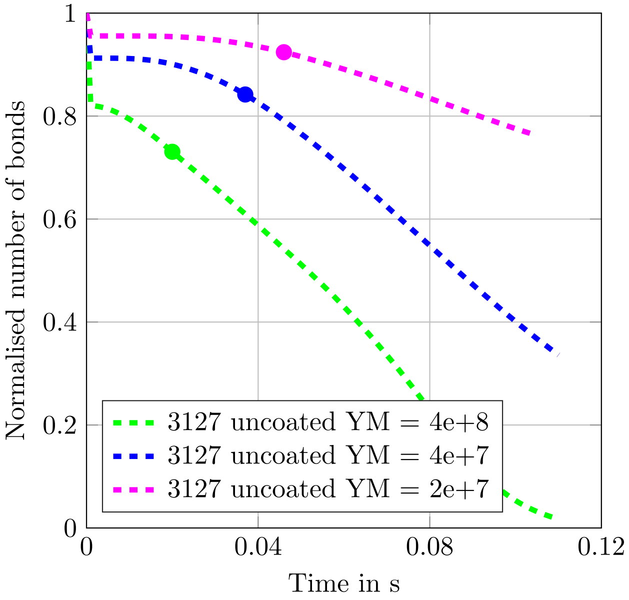

Fig. 18 Change in relative number of bonds during the MPT simulation of uncoated Poraver® particles

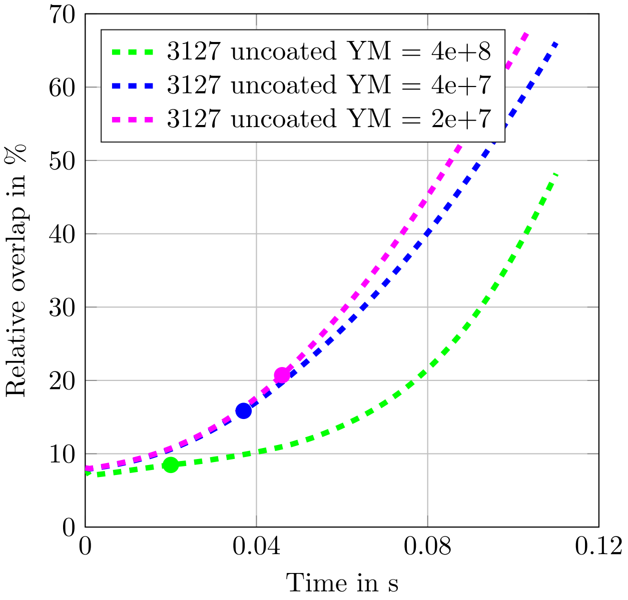

Fig. 19 Change in relative overlap during the MPT simulation of uncoated Poraver® particles

experiments, the Young's modulus is halved again to 20 MPa. Consequently, fewer bonds are broken, and more softening occurs, highlighted by the magenta curves in Figs. 18 and 19. The results now better match the experimental data in Fig. 17. However, a significant reduction in Young's modulus is not ideal. As the particles soften and overlap increases, there comes a point where contact forces are too weak to resist the compression force. As a result, particles penetrate the rigid surface and eventually leave the simulation domain (i.e. the cylinder). This issue is observed in the magenta curve in Fig. 17, where the results terminate around 42% strain. Beyond this point, the simulation becomes unstable. Furthermore, more compression is needed before the stress threshold is reached, as seen in the magenta markers in Figs. 18 and 19.

Nevertheless, the two-step approach used for the coated particles is effective for uncoated particles as well, where the numerical model accurately simulates micro-cracking behaviour. When extended to MPT, strains up to 10% are reasonably well captured, although parameter adjustments are needed to improve agreement beyond that range.

7 Conclusion

This paper presented the use of the discrete element method (DEM) combined with the bonded particle method (BPM) to predict the compressive behaviour of coated particles. To represent the microstructure on mesoscale, they were modelled as clusters of smaller particles bonded together. An elasto–plastic bond model incorporating micro-cracking was employed. Additionally, a comparison was made between a high-fidelity (HF) and a low-fidelity (LF) modelling approach. The HF model included an additional layer of smaller particles surrounding the core to replicate the coating behaviour, whereas the LF model neglected the coating and approximated the bulk response by extending the core region. This simplification significantly reduced the number of particles, bonds, and more importantly, the number of parameters to be identified.

Once both agglomerate structures were defined, a sensitivity analysis and particle swarm optimisation (PSO) algorithm were applied to the single particle compression test (SPT), which is computationally less demanding. An average force-displacement curve was constructed and used as the objective function for optimisation. A total of seven parameters for HF and two LF were optimised.

The optimised models were then validated against experimental SPT results. The bond model successfully captured the micro-cracking behaviour observed in physical particles, and both HF and LF models reproduced the nonlinear force-displacement relationship. Despite having fewer particles, bonds, and parameters, the LF model produced results that closely matched both the experimental average and the HF model. Minor differences were observed in initial stiffness and peak force, but all simulations remained within the experimental variability.

Additionally, two HF setups, HF-A and HF-B, were compared based on distinct optimised parameter sets. While both fell within the experimental range, the HF-A model qualitatively aligned better with the observed behaviour. This underlined the importance of selecting appropriate parameter bounds to ensure that simulation results reflect the physical particle crushing behaviour.

In the multi particle compression test (MPT), the HF model could not replicate the full number of physical particles due to GPU memory limitations. Nevertheless, simulations with over 50% of the physical particle count were conducted. In contrast, the LF model enabled simulations with a greater number of agglomerates, leading to a better match with the bulk stress–strain response observed experimentally up to 20% strain, particularly when the setup included pre-compression. It was found that excessive overlap, exceeding 2–4% of the particle diameter, violates the assumptions of the Hertz–Mindlin contact model and results in notable stress increase after 20% strain. This effect was mitigated by reducing Young's modulus of particles 10 ×, which allows for softer contact interactions. Consequently, the results match better with the experiments.

A key advantage of the LF approach lies in its computational efficiency. Simulations demonstrated a speed-up of 1.4 in SPT and 3.3 in MPT, with potential for even greater improvements in large-scale simulations. These results suggest that the LF model offers a reliable and computationally efficient alternative for large-scale DEM-BPM simulations, enabling broader parametric studies and practical use in engineering applications with limited computational resources. However, even with the LF approach, the scale of the simulated MPT remains roughly 5000 × smaller than that of a typical double hull structure. At such scales, the LF model still qualifies as a detailed model capable of capturing bulk compressive behaviour, provided that proper parameter calibration is performed. Nevertheless, for full-scale applications, additional modelling strategies such as FEM-DEM coupling may be necessary to achieve feasible simulation runtimes.

To provide further validation to the two-step approach previously applied to coated particles was successfully extended to uncoated Poraver® particles. The numerical model provided reasonable agreement with both SPT and MPT results, particularly up to 10% strain in the latter. The micro-cracking and energy dissipation behaviour were well captured by the bond model. Nevertheless, parameter adjustments are required in the MPT to ensure the model remains applicable for larger-scale simulations. Ideally, parameter optimization would be performed directly on the multi particle compression tests; however, due to the high computational cost, a compromise between accuracy and effort is necessary. In this context, the two-step approach along with LF model for coated particles offers a practical and sufficiently accurate solution.

Acknowledgements The presented research is funded by the German Research Foundation (Deutsche Forschungsgemeinschaft, DFG) in the framework of the research training group GRK 2462 "Processes in natural and technical Particle-Fluid-Systems" (PintPFS), which is gratefully acknowledged.

Funding Open Access funding enabled and organized by Projekt DEAL.

Declarations

Conflict of interest The authors declare that they have no conflict of interest.

References

1. Brown NJ, Chen JF, Ooi JY (2014) A bond model for dem simulation of cementitious materials and deformable structures. Granul Matter 16(3):299–311. https://doi.org/10.1007/s10035-014-0494-4
2. Chaudry M, Woitzik C, Düster A, Wriggers P (2018) Experimental and numerical characterization of expanded glass granules. Comput Particle Mech 5(3):297–312. https://doi.org/10.1007/s40571-017-0169-0
3. Chaudry M, Woitzik C, Düster A, Wriggers P (2022) A multiscale dem–fem coupled approach for the investigation of granules as crash-absorber in ship building. Comput Particle Mech 9:179–197. https://doi.org/10.1007/s40571-021-00401-5
4. Chaudry M, Woitzik C, Weißenfels C, Düster A, Wriggers P (2016) Dem-fem coupled numerical investigation of granular materials to increase crashworthiness of double-hull vessels. PAMM 16(1):311–312. https://doi.org/10.1002/pamm.201610144
5. Cundall P, Strack O (1979) A discrete numerical model for granular assemblies. Géotechnique 29(1):47–65. https://doi.org/10.1680/geot.1979.29.1.47
6. Dosta M, Skorych V (2020) Musen: an open-source framework for gpu-accelerated dem simulations. SoftwareX 12:100618. https://doi.org/10.1016/j.softx.2020.100618
7. Etikan MK, Jelagin D, Olsson E, Partl MN (2024) Experimental and numerical analyses of crushing resistance of unbound road materials. Int J Pavement Eng. https://doi.org/10.1080/10298436.2024.2330630
8. Jahn M, Meywerk M (2024) On the sensitivity of dem parameters on pile experiments. Comput Particle Mech 11(6):2971–2993. https://doi.org/10.1007/s40571-024-00769-0
9. Kennedy J, Eberhart R (1995) Particle swarm optimization. In: Proceedings of the IEEE international conference on neural networks, vol 4, pp 1942–1948. https://doi.org/10.1109/ICNN.1995.488968. (**IEEE**)
10. Ma J, Sun Q, Liu S, Yang X (2024) Experimental study of energy-absorbing and support characteristics of glass microsphere-

filled steel tube columns under uniaxial compression. Sci Rep 14(1):4801. https://doi.org/10.1038/s41598-024-55562-z

11. Mindlin RD, Deresiewicz H (1953) Elastic spheres in contact under varying oblique forces. J Appl Mech 20(3):327–344. https://doi.org/10.1115/1.4010702
12. Museum of Fine Arts, Boston (2023) Candelilla wax. https://cameo.mfa.org/wiki/Candelilla_wax . Online accessed 24 Mar 2025
13. New KCB, Watt K, Misner CW, Centrella JM (1998) Stable 3-level leapfrog integration in numerical relativity. Phys Rev D 58(6):064022. https://doi.org/10.1103/PhysRevD.58.064022
14. Orth M, Rotter S, Safdar W, Tasdemir S, Pietsch-Braune S, Heinrich S, Düster A (2023) Fluidized bed spray coating for improved mechanical properties of particles. Processes. https://doi.org/10.3390/pr11020314
15. O'Sullivan C, Bray JD (2004) Selecting a suitable time step for discrete element simulations that use the central difference time integration scheme. Eng Comput 21(234):278–303. https://doi.org/10.1108/02644400410519794
16. Pan X, Niu Y, Zhao Y, Huang P, Wu Y (2023) Parameter calibration method of clustered-particle logic concrete dem model using bp neural network-particle swarm optimisation algorithm (bp-pso) inversion method. Eng Fract Mech 292:109659. https://doi.org/10.1016/j.engfracmech.2023.109659
17. Poraver: Poraver® website (2022) https://poraver.com/en/poraver/ (2022). Online; accessed: 2025-04-10
18. Potyondy D, Cundall P (2004) A bonded-particle model for rock. Int J Rock Mech Min Sci 41(8):1329–1364. https://doi.org/10.1016/j.ijrmms.2004.09.011
19. Potyondy DO (2007) Simulating stress corrosion with a bonded-particle model for rock. Int J Rock Mech Min Sci 44(5):677–691. https://doi.org/10.1016/j.ijrmms.2006.10.002
20. Prasad BB, Duvigneau F, Reinboth T et al (2024) Design strategies of particle dampers for large-scale applications. J Vib Eng Technol 12:5715–5746. https://doi.org/10.1007/s42417-023-01214-x
21. Quentrec B, Brot C (1973) New method for searching for neighbors in molecular dynamics computations. J Comput Phys 13(3):430–432. https://doi.org/10.1016/0021-9991(73)90046-6
22. Rotter S, Dosta M, Düster A (2023) Discrete element simulation of the breakage behavior of porous granules utilizing bond models. Comput Particle Mech. https://doi.org/10.1007/s40571-023-00610-0
23. Schöttelndreyer M, Lehmann E, Thieme C, Greulich M (2014) Multizellulare glashohlkugeln zur verstärkung von doppelhüllen in der schiffskonstruktion. In: Proceedings of the ANSYS conference & 32. CADFEM user's meeting. Nürnberg, Germany
24. Schöttelndreyer, M (2015) Füllstoffe in der konstruktion: Ein konzept zur verstärkung von schiffsseitenhüllen. Ph.D. thesis, Technische Universität Hamburghttps://doi.org/10.15480/882.1258
25. The MathWorks, Inc (2024) Optimization toolbox user's guide. https://www.mathworks.com/products/optimization.html. Version R2024a. Online; accessed: 2025-04-27
26. Tsuji Y, Tanaka T, Ishida T (1992) Lagrangian numerical simulation of plug flow of cohesionless particles in a horizontal pipe. Powder Technol 71(3):239–250. https://doi.org/10.1016/0032-5910(92)88030-L
27. Verlet L (1967) Computer experiments on classical fluids. I. Thermodynamical properties of Lennard–Jones molecules. Phys Rev 159(1):98–103. https://doi.org/10.1103/PhysRev.159.98
28. Wang M, Lu Z, Wan W, Zhao Y (2021) A calibration framework for the microparameters of the dem model using the improved pso algorithm. Adv Powder Technol 32(2):358–369. https://doi.org/10.1016/j.apt.2020.12.015
29. Woitzik C (2021) Experimental testing and numerical simulation of granules as crash absorber for double hull structures. Ph.D. thesis, Technische Universität Hamburg https://doi.org/10.1016/j.apt.2020.12.015
30. Woitzik C, Düster A (2017) Modelling the material parameter distribution of expanded granules. Granul Matter 19(3):52. https://doi.org/10.1007/s10035-017-0735-4
31. Wolf FP (1979) Präzisionsmessungen des elastizitätsmoduls von polymeren mit longitudinalschwingungen. Colloid Polym Sci 257(11):1133–1158. https://doi.org/10.1007/BF01517239
32. Wriggers P, Avci B (2020) Discrete element methods: basics and applications in engineering. In: De Lorenzis L, Düster A (eds) Modeling in engineering using innovative numerical methods for solids and fluids. Springer, Cham, pp 1–30. https://doi.org/10.1007/978-3-030-37518-8_1